THz acoustic phonon spectroscopy and nanoscopy by using piezoelectric semiconductor heterostructures

Pierre-Adrien Mante [a], Yu-Ru Huang [a], Szu-Chi Yang [a], Tzu-Ming Liu [b], Alexei A. Maznev [c], Jinn-Kong Sheu [d], Chi-Kuang Sun [a,e,f,*]

[a] Department of Electrical Engineering and Graduate Institute of Photonics and Optoelectronics, National Taiwan University, Taipei 10617, Taiwan
[b] Institute of Biomedical Engineering, National Taiwan University, Taipei 10617, Taiwan
[c] Department of Chemistry, Massachusetts Institute of Technology, Cambridge, MA 02139, USA
[d] Institute of Electro-Optical Science and Engineering and Advanced Optoelectronic Technology Center, National Cheng Kung University, Tainan 70101, Taiwan
[e] Molecular Imaging Center, National Taiwan University, Taipei 10617, Taiwan
[f] Institute of Physics and Research Center for Applied Sciences, Academia Sinica, Taipei 115, Taiwan

ARTICLE INFO

ABSTRACT

Thanks to ultrafast acoustics, a better understanding of acoustic dynamics on a short time scale has been obtained and new characterization methods at the nanoscale have been developed. Among the materials that were studied during the development of ultrafast acoustics, nitride based heterostructures play a particular role due to their piezoelectric properties and the possibility to generate phonons with over-THz frequency and bandwidth. Here, we review some of the work performed using this type of structure, with a focus on THz phonon spectroscopy and nanoscopy. First, we present a brief description of the theory of coherent acoustic phonon generation by piezoelectric heterostructure. Then the first experimental observation of coherent acoustic phonon generated by the absorption of ultrashort light pulses in piezoelectric heterostructures is presented. From this starting point, we then present some methods developed to realize customizable phonon generation. Finally we review some more recent applications of these structures, including imaging with a nanometer resolution, broadband attenuation measurements with a frequency up to 1 THz and phononic bandgap characterization.

Contents

* Corresponding author.
   E-mail address: sun@ntu.edu.tw (C.-K. Sun).

0. Introduction

Since its invention by Maris in the beginning of the eighties [1,2], the picosecond ultrasonic technique has developed into a complete technique able to study various phenomena from thickness measurements [3,4] to hypersound attenuation [5,6]. Based on the use of an ultrafast laser, this technique allows the generation and detection of coherent acoustic phonons (CAP) in the sub-THz range.

The generation of CAP can be occurring due to multiple mechanisms when a femtosecond laser pulse is absorbed by a material. The most common ones are often due to thermoelasticity [2,7] or coupling through deformation potential [8,9]. However, other mechanisms can be responsible for the generation of CAP, such as piezoelectricity [10–13]. In that case, the excited electrons and holes, due to the absorption of a femtosecond light pulse, are spatially separated due to the piezoelectric field, resulting in a space-charge density. This space charge density screens the piezoelectric field and instantaneously modifies the lattice equilibrium. Then the lattice relaxes and initiates the generation of CAP. This technique has been efficiently applied to nitride based semiconductor heterostructures, like quantum wells. With a width as small as 3 nm, CAP in the THz range, providing extreme sensitivity, have been generated [14].

In this article, we present a review of the CAP work that has been performed on InGaN/GaN piezoelectric heterostructures, with a focus on its capability to perform phonon nanoscopy and THz acoustic phonon spectroscopy in solids. First, we will briefly introduce the theory behind the generation and detection of CAP through piezoelectric effect in wurtzite materials for different orientations. Then we will not only present some experimental observation of the CAP generated by these structures, but also some more advanced technique to realize acoustic pulse shaping. Finally, we will show applications of these THz piezoelectric acoustic transducers to acoustic nanoscopy imaging and the study of THz sound attenuation.

1. Theory

In this section, we introduce the model for the generation of CAP by wurtzite nitride based semiconductor heterostructures, like quantum wells [10,15]. The model is based on the macroscopic constitutive equations taking into account both the piezoelectric and deformation potential couplings. The governing dynamical equations are the elastic wave equations coupled to the Poisson's equation. A complete microscopic description of the problem can be found elsewhere [16].

First, let us consider that the growth direction of the quantum well structure can be different from the c-axis, we therefore need to introduce two sets of coordinates. The first one, (x,y,z), corresponds to the crystallographic axes of wurtzite nitrides with $[x_1 = \bar{1}\,\bar{1}\,2\,0]$, $x_2 = [1\,\bar{1}\,0\,0]$ and $x_3 = [0\,0\,0\,1]$ as depicted in Fig. 1. In the second coordinates, (x',y',z'), related to the growth direction of the heterostructure, we have $x'_3 = \hat{n}$, $x'_2 = x_2$ and x'_1 perpendicular to x'_2 and x'_3. The angle between the c-axis and the growth direction is θ.

In the following, we will consider thermoelastic generation to be negligible compared to piezoelectric and deformation potential effects. This condition is often verified experimentally when the

laser energy is close to the band gap of the semiconductor. With this assumption, the stress tensor and the electric displacement are given by:

$$\sigma_{ij} = C_{ijkl}\epsilon_{kl} - e_{kij}E_k + \sum_{v=e,h}\delta_{ij}d_v\rho_v, \tag{1}$$

$$D_i = \varepsilon_{ij}E_j + e_{ikl}\epsilon_{kl}, \tag{2}$$

where ϵ_{kl} is the strain tensor and $E = (E_x, E_y, E_z)$ is the electric field. C_{ijkl}, ε_{ij}, and e_{ikl} are the stiffness, dielectric, and piezoelectric tensor, respectively. The stress also has a contribution from deformation potential coupling, which is represented by the last term of σ_{ij}. d_v is the deformation potential constants for species v, and ρ_v, is the carrier density of species v.

In our study, the well and its barriers are very similar due to the low In composition of the well, we can therefore, as a first approximation, neglect the discontinuities of elastic and dielectric properties. The equation of motion thus becomes:

$$\rho_0\frac{\partial^2 u_i}{\partial t^2} = \frac{\partial \sigma_{ij}}{\partial x_j}, \tag{3}$$

where ρ_0 is the mass density and u is the displacement vector field. The electric displacement D satisfies the Poisson equation

$$\nabla.D = \rho_{SC} = |e|(\rho_{\text{hole}} - \rho_{\text{elec}}), \tag{4}$$

where ρ_{SC} is the space charge density. Due to the experimental geometry, the space charge density varies along the growth direction of the MQW and therefore depends only on the variable z'. Assuming $E = E_{SC}\hat{n}$, we obtain:

$$\bar{\varepsilon}\frac{\partial E_{sc}}{\partial z'} = \rho_{SC} - \bar{e}.\frac{\partial^2 u}{\partial z'^2}. \tag{5}$$

To take into consideration the difference between the growth and the c-axis, we introduce the effective dielectric function $\bar{\varepsilon}(\theta)$, the effective piezoelectric coefficients $\bar{e}$, the effective second-rank Christoffel tensor Γ and the first-rank tensor of the effective deformation potential $\bar{d}_v$ along the growth direction defined by:

$$\bar{\varepsilon}(\theta) = \varepsilon_1 \sin^2(\theta) + \varepsilon_3 \cos^2(\theta), \tag{6}$$
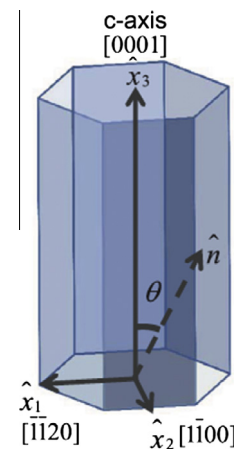
Fig. 1. Coordinate adopted to express the effective piezoelectric constants (adapted from Ref. [22]).

$$\bar{e}_k = e_{ijk}N_iN_j, \tag{7}$$

$$\bar{\Gamma}_{il} = C_{ijkl}N_jN_k + \frac{\bar{e}_i\bar{e}_l}{\bar{\varepsilon}}, \tag{8}$$

$$\bar{d}_{vi} = d_iN_i. \tag{9}$$

By substituting the expression of the stress (Eq. (1)) and the spatial derivative of the electric field (Eq. (5)) in the equation of motion, we obtain:

$$\rho_0 \frac{\partial^2 u}{\partial t^2} - \bar{\Gamma} \cdot \frac{\partial^2 u}{\partial z'^2} = f_{piezo} + f_{def}. \tag{10}$$

The two driving forces, which are due to deformation potential and piezoelectricity are:

$$f_{piezo} = |e|\frac{\bar{e}}{\bar{\varepsilon}}(\rho_{elec} - \rho_{hole}), \tag{11}$$

and

$$f_{def} = \sum_v \bar{d}_v \frac{\partial \rho_v}{\partial z'}. \tag{12}$$

While Eq. (12) tells us that deformation potential only contributes to the generation of longitudinal waves, *i.e.* the displacement is in the same direction as the propagation, we can see from Eq. (11) that the piezoelectric driving force is in the same direction as the effective piezoelectric tensor, which means that it is possible, depending on the angle θ between c-axis and the growth direction, to generate longitudinal and transverse waves. In the case of GaN with 6 mm symmetry, the effective piezoelectric constants for LA and TA modes can be expressed as:

$$\bar{e}_{LA} = \left[(2e_{24} + e_{32})\sin^2(\theta) + e_{33}\cos^2(\theta)\right]\cos(\theta), \tag{13}$$

$$\bar{e}_{TA} = \left[(e_{24} + e_{32} + e_{33})\cos^2(\theta) - e_{24}\sin^2(\theta)\right]\sin(\theta). \tag{14}$$

To solve Eq. (10), we first need to find a solution to the equation without the driving forces by finding the eigenmodes of the Christoffel tensor. The CAPs are then written as linear superposition of these eigenmodes. The driving forces are obtained by projecting the general force densities onto the directions of the eigenmodes.

2. Experiments

After looking at the theory of the generation of coherent acoustic phonons by piezoelectric quantum wells, we are now discussing some experimental results. In a first time, we will present some

results on the generation of longitudinal CAP by multiple quantum well (MQW) and single quantum well (SQW) structures, and of shear waves with oriented MQW. Then we will discuss some more advanced features of the generation of CAP by piezoelectric quantum wells, such as coherent control and filtering.

2.1. Generation

2.1.1. Multiple quantum well

Generation of CAP by piezoelectric MQW using femtosecond laser pulses has been observed by using InGaN/GaN structure [17–19]. In other materials exhibiting piezoelectricity, similar results have been obtained [11,12]. In this paper, a new set of samples geometries, whose structures were carefully characterized by using transmission electron microscopy (TEM), was studied. In each case, the GaN barrier width was varied from 30 to 90 Å and the InGaN well width was varied from 22 to 62 Å, corresponding to a change in periodicity from 50 to 112 Å. In all samples, the MQW was composed of 14 periods and the indium composition was controlled at 10%. Using femtosecond pump probe spectroscopy with a pump energy above the bandgap of the well, and a similar probe energy to monitor the absorption changes in the well, the generation of CAP was observed within the first 20 ps, as shown in Fig. 2.

In this study, the influence of the period on the generated frequencies is verified. It is worth mentioning that due to the relatively weak acoustic impedance mismatch (2.4%) between GaN and $In_{0.1}Ga_{0.9}N$, the number of oscillations, which is equal to the number of MQW, can be clearly identified when the CAPs are propagating outwards [19]. From the theoretical model, the angular frequency is given by $\omega = 2\pi c/P = qc$, where c is the effective sound velocity, P is the period of the MQW system and q is the phonon wavevector. Therefore, the phonon frequency should depend linearly on the phonon wavevector as it is observed experimentally as summarized in Fig. 3. The experimentally obtained effective sound velocity, as determined in Fig. 3, 7350 m s^{-1} is in very close proximity to the longitudinal sound velocity along c-axis in GaN [20], confirming the acoustic nature of this excitation. The measured lower value could be a result of the average of sound velocity in $In_{0.1}Ga_{0.9}N$ wells and GaN barriers. In addition to the linear dependence between the wavevectors q and angular frequencies ω, the CAP oscillations had a cosine nature confirming the piezoelectric origin of the displacement excitation.

2.1.2. Single quantum well

While in MQWs, CAPs at specific frequency are generated due to the periodicity of the structure, in SQW, a broadband CAP can be
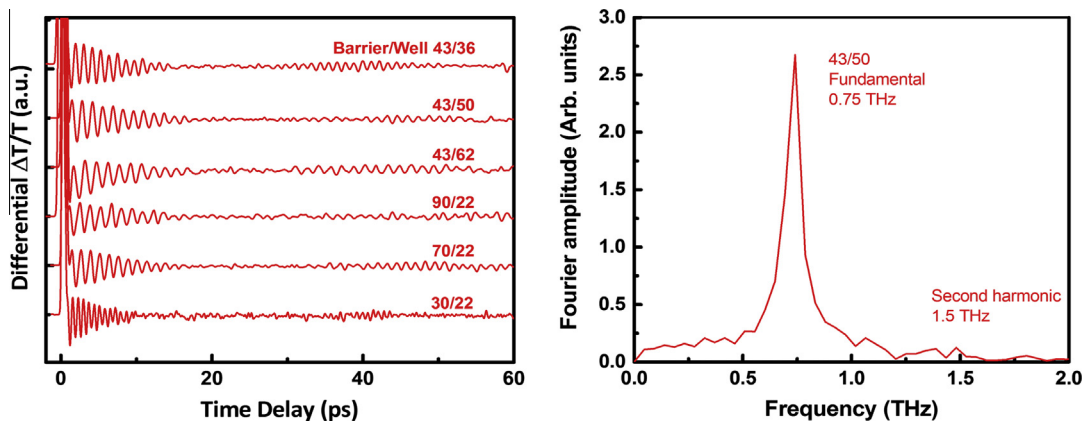
Fig. 2. Normalized transient transmission changes versus probe delay for different MQWs. Traces are vertically displaced for clarity.

generated. Using a 3 nm thick InGaN single quantum well with a GaN cap layer of 70 nm, we obtain the transient transmission changes depicted in Fig. 4.

A structure can be observed around 18 ps on this trace or on the background removed transient transmission in the inset. This contribution corresponds to the round trip of a femtosecond acoustic pulse generated in the SQW and reflected by the free surface. By using a sound velocity of 7960 m s^{-1} [21], we obtain a cap layer thickness of 71 nm in good agreement with the expected value. By performing the Fourier transform of this echo, we observe a spectrum with broad bandwidth, up to 1 THz, even after suffering surface scattering and propagation losses.
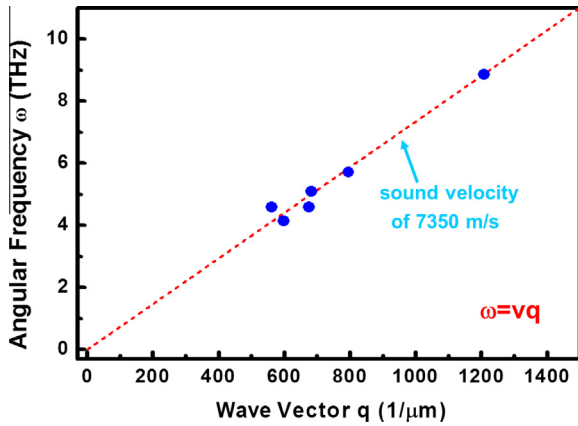
We have seen that piezoelectric SQW and MQW allow the generation of CAPs. Interestingly, these two different structures are complimentary and, used together, allows the study of a sample in an extremely wide range of frequency. Indeed, while MQWs can only generate CAPs at a specific frequency, the CAPs are detected two times, when they are generated and when they propagate back to the MQWs structure (as shown in Fig. 2, around 40 ps), which allows realizing normalization. For example, if we want to study the attenuation, using MQW, we can directly observe the losses by comparing the generated CAPs to the one detected after propagation. On the other hand, SQW offers the possibility to study a broad range of frequency. However, the generated acoustic signal cannot be observed. It is thus interesting to study a phenomenon using both SQW and MQW structure.

2.1.3. Shear waves

In the first section, we have seen that it is possible to generate shear waves by wisely choosing the angle θ between the growth direction of the structure and the *c*-axis. Recently, the generation of shear waves by MQW structure using this principle has been demonstrated [22]. In this work, MQW were grown along the direction perpendicular to the *c*-axis (*m*-plane). From Eqs. (13) and (14), we can see that no longitudinal CAP should be generated, only transverse ones. In Fig. 5, we show the transient transmission change obtained on this structure.

Oscillations were observed and by performing the Fourier transform, we can obtain the frequency of this signal, 0.4 THz. A period of 12.2 nm was measured for this structure, which leads to a sound velocity of 4880 m s^{-1}, in good agreement with the sound velocity of transverse waves in GaN [23].

Fig. 3. Angular frequency versus wave vector. A linear dispersion is observed.
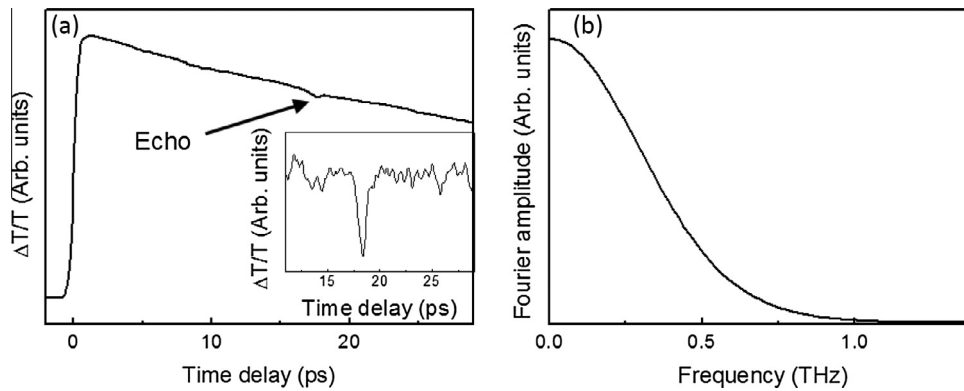
Fig. 4. (a) Transient transmission change obtained with a 3 nm SQW sample capped with a 70 nm thick layer. Inset: transient transmission change after removal of the background. (b) Fourier transform of the acoustic echo signal.
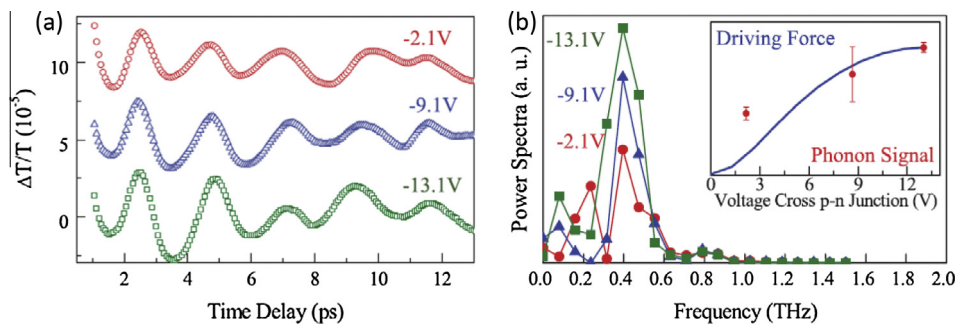
Fig. 5. (a) Transient transmission change obtained on m-plane MQW with Background-removed to display the TA phonon oscillations for different voltage. (b) Corresponding Fourier power spectra of pump probe signal. The red dots in the inset are the pick values of the Fourier power spectra for different voltage jumps (adapted from Ref. [22]). (For interpretation of the references to color in this figure legend, the reader is referred to the web version of this article.)

2.2. Coherent control and waveform synthesis

The generation of THz CAP by piezoelectric heterostructures has been demonstrated, and some more advanced features of this generation have also been studied. In order to apply CAP to a specific purpose, like dynamic focusing imaging or to use them as modulators, it is important to control its waveform properties, such as the phase or the frequency. In the following, we are going to present different experimental methods designed to control the generated CAP.

2.2.1. Phase control

A widespread method of temporal phase control, known as coherent control, is performed by using two or more laser pulses
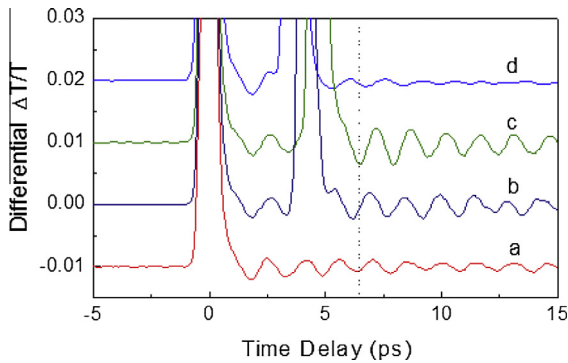
Fig. 6. The differentiated transmission changes versus probe delay with (b)–(d) and without (a) the control pulse. The experiments were performed in the 62 Å InGaN MQW sample. Oscillation phase shifts of −20° (trace b), +35° (trace c), and +135° (trace d) were achieved with the control pulses (adapted from Ref. [34]).

with controllable delay and amplitude ratio. This technique has already been used to control numerous phenomena like molecular motion [24], electronic quantum dynamics [25,26], electron–phonon scattering, [27] photocurrent generation in semiconductors [28]. The same principle has been used to control the phase and amplitude of CAPs [29–33]. Here, we present how these methods have been applied to control CAPs generated by piezoelectric MQW structure [34]. The amplitude control with the same phase can be considered as a coherent amplification process for acoustic phonons. An interesting coherent amplification finding was reported in a previous literature [35].

In this study, the experimental setup is almost similar to the classical femtosecond pump–probe spectroscopy one. The main difference is the separation of the pump in two parts. These two pumps have similar incidence angle to have the maximum overlap. The time delay between these two beams was controlled by a delay stage and the ratio of intensities by neutral density filters. Thanks to these two pump impulses, it is possible to perform coherent control. In Fig. 6, we reproduce the experimental traces obtained on a InGaN MQW sample with well width of 62 Å and barrier width of 43 Å, with an intensity ratio of 1.15 at different time delay.

One observes that when the second pulse is introduced, CAP signal is modified. First, the amplitude of the signal can be varied. For example, if the time delay between the two pulses is a multiple to the period of the CAP, then the signal can be enhanced. Another interesting feature is the control of the phase, as can be seen one the figure by using the dashed line as a guide for the eye. By varying the delay and intensity ratio, a complete ±180 phase shift was achieved.

By wisely designing the MQW structure, it is also possible to shape and control the CAP. Indeed, when carriers are photoexcited in the MQW structure, they will subsequently generate two CAPs
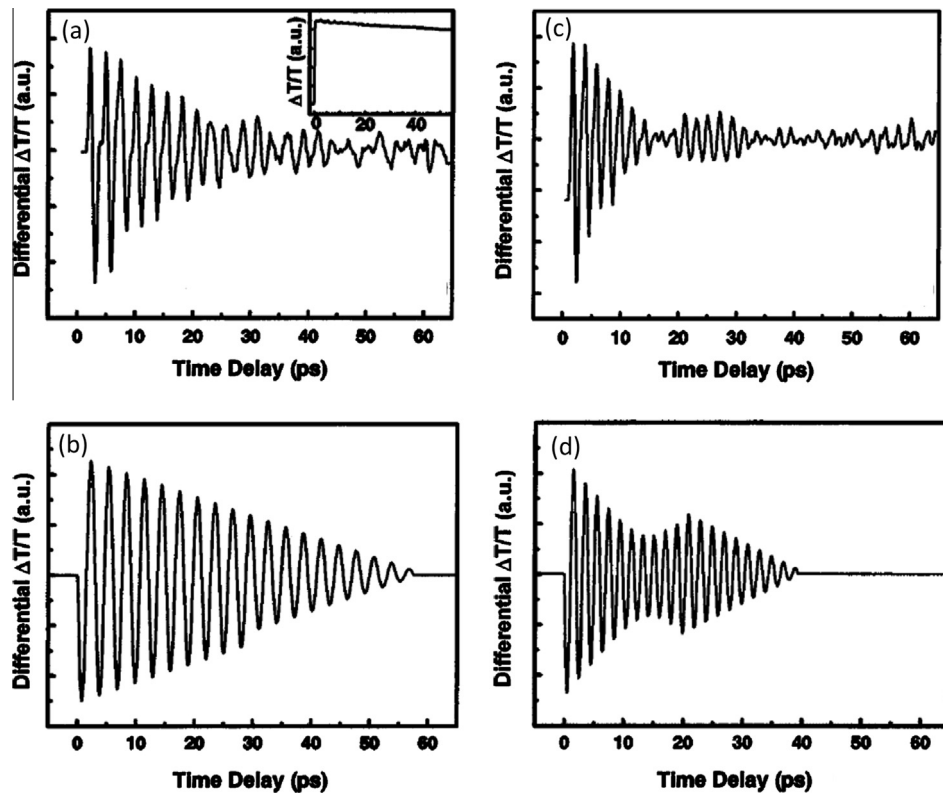
Fig. 7. (a) Differentiated trace of the measured optical transient transmission of first sample, showing a prolonged coherent oscillation. (b) Corresponding theoretical simulation. (c) Differentiated trace of the measured optical transient transmission of the second sample, showing a phase change of 240°. (d) Corresponding theoretical simulation (adapted from Ref. [36]).
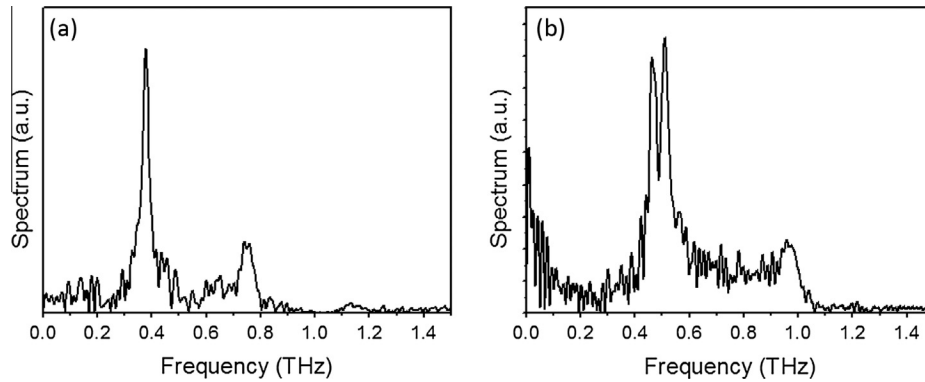
Fig. 8. (a) Fourier transform of the transient transmission measured in the first sample. (b) Fourier transform of the transient transmission measured in the sample with a 245° phase shift.

propagating in counter directions. The basic idea to control the shape is to reflect one of this CAP and makes it interact with the other. By wisely choosing the distance the CAP propagates before reflection, it is possible to choose the phase difference between the two CAPs, or even to modify its frequency components as will be shown in the later discussion (Fig. 8) [36].

To demonstrate this possibility two samples have been designed. The first one contains a 10 periods 2.9/21.7 nm $In_{0.23}Ga_{0.77}N$/GaN MQW capped with a 4.7 nm GaN cap layer. The second sample also contains a 10 period MQW but the thicknesses of $In_{0.23}Ga_{0.77}N$ and GaN are respectively 2.9 and 13 nm and the cap layer is 7.9 nm. In these samples, the GaN/air interface plays the role of the mirror. Given the acoustic mismatch between GaN and air, an almost total reflection is obtained and a 180° phase shift is observed. The wavelength, λ, of the CAP generated by the MQW being given by the period of the structure, the distance from the middle of the first well to the GaN/air interface corresponds to 1/4 λ for the first sample and 0.59 λ for the second one. Fig. 7 shows the transient transmission changes measured in both samples and the original simulation-expected waveform.

First we can see that when the distance from the first well to the GaN/air interface is 0.25 λ, the signal decreases linearly. When the CAPs do a round trip in the cap layer, they travel a distance equals to 0.5 λ, which corresponds to a 180° shift, and the reflection at the free surface brings another 180° shift, therefore both CAP (the one propagating towards the substrate and the one reflected from the surface) are in phase, which explain the observe linear decrease. In the second sample, the expected phase shift between these two CAP is 245°. We can observe experimentally that the first decrease is much faster as the reflected CAP interferes with the propagating one. As time evolves, the initial CAPs leave the MQW and the reflected ones are detected. In both cases, a good agreement is observed between experiments and simulations. This method not only allows to synthetize a strain shape in the time domain, but also in the frequency domain, as can be seen from the Fourier transform of both signals reproduced in Fig. 8. As can be observed in Fig. 8(a), with a limited quantum well numbers, the resulted CAP is with a finite bandwidth. By manipulating the phase between two CAP, we are able to decrease the amplitude of the central frequency component and resulted in a modification of the frequency spectrum, as shown in Fig. 8(b). This spectrum can also be understood as the measurement of the defect phonon state being introduced by the cap spacing layer in a phononic bandgap structure.

Control of the phase will enable the use of CAP in multiple new applications. Indeed, electronic or optical behaviors of materials can be modified by strain [37]. The control of the phase will lead to enhanced precision on the control of these properties. In addition,

control of the phase would allow us to remotely control the state of interference between two acoustic waves. This phenomenon could be extremely important for multiple applications, such as imaging [38] and sasers [35,39].

2.2.2. Frequency control

As we have seen previously, SQW structure allows the generation of CAPs with a broad spectrum extending to 1 THz. However, it is possible to enhance the signal at a specific frequency. In MQWs, we are able to generate CAPS at a specific frequency dictated by the period of the MQW, in other words, CAPs with broad spectrum are generated by each quantum well, but due to the spatial periodicity, an almost monochromatic CAP is observed. Using SQW, we can generate CAPs at specific frequency using a periodic repetition of laser pulse in the time domain [40].

In this work, two samples were used. In the first one, an InGaN well with a width of 7 nm is capped by a 60 nm thick GaN layer, while the other sample has a well with a width of 2.9 nm and a cap layer of 70 nm. For the generation, an optical pulse train, containing three pulses, is directed towards the sample. The time delay between the three pulses can be controlled thanks to the use of delay stages. In Fig. 9, we reproduce, for each sample, three transient transmission changes for different delays between the pump pulses.

On these traces, we can observe some oscillations at specific frequencies, dictated by the delay between the different pump pulses. It becomes thus possible using a SQW, to tune the frequency in the sub-THz range. This application can be interesting when the study of phenomena requires working at specific frequency: even though a SQW sample could generate this frequency, the signal to noise ratio can be greatly enhanced using this technique.

Control over the frequency of the generated CAP can also be achieved by using MQW. Indeed, when the barrier and well thicknesses are different, the generated waveform is not sinusoidal. When expanding this periodic strain waveform into different frequency components, multiple harmonics can be observed. Taking advantage of this principle, it is then possible, through coherent control, to specifically generate one of these frequencies [41]. For example, we have a MQW structure of 14 periods with well and barrier width of 2.2 and 7 nm, respectively. Fig. 10(a) shows the differential transmission with a pump energy above the band gap of the well.

By doing the Fourier transform of this signal, we can observe multiple frequencies, 0.8, 1.6 and 2.4 THz, corresponding to the fundamental, second and third harmonic, respectively. Here, we show one example to illustrate the concept of waveform synthesization, which is to control the phase and amplitude of different acoustic frequency component to manipulate the final acoustic
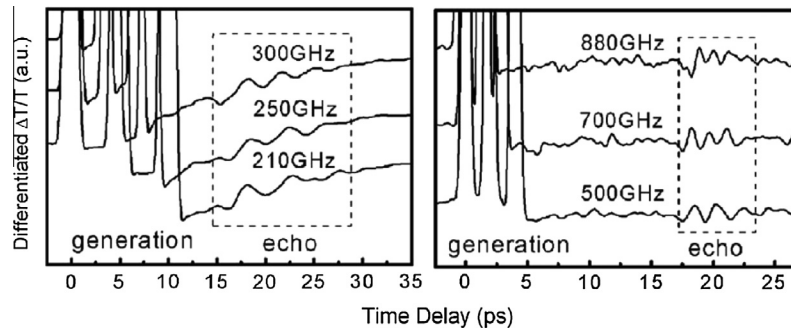
Fig. 9. Differentiated transient transmission measurement demonstrates the optical coherent control of the generated acoustic frequency in the 7 nm thick and 2.9 nm thick InGaN SQW (adapted from Ref. [40]).
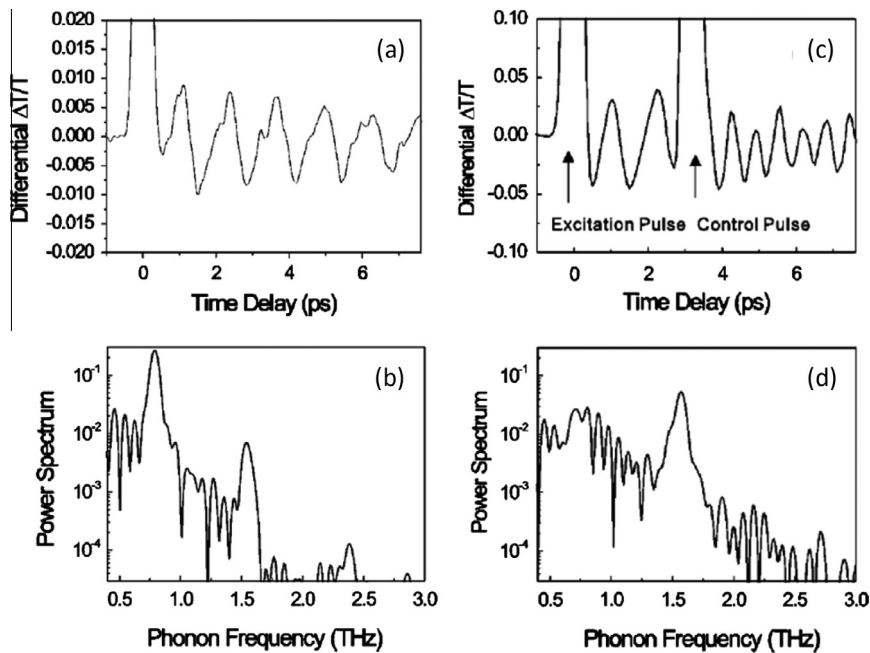
Fig. 10. (a) Measured differential transmission change versus probe delay for a 22 Å/70 Å InGaN/GaN MQW. The modulated transmission change with a period of 1.27 ps reflects the photoinduced coherent acoustic phonon oscillation. The laser wavelength was 390 nm. (b) Fourier power spectrum of the temporal trace. (c) Measured differentiated transmission changes versus probe delay with a control pulse at 2.5 fundamental oscillation cycles after the first pump pulse. Second-harmonic oscillation with a period of 0.63 ps can be clearly observed after applying coherent control with a control pulse. (d) Fourier power spectra of the temporal trace (adapted from Ref. [41]).

waveform. Here we use a control pulse that is delayed by 2.5 times the fundamental period. It corresponds to a delay of 5 times the second harmonic and 7.5 times the third harmonic. As a result, the CAPs generated by the control pulse are out of phase for the fundamental and third harmonic, which are interfering destructively, and in phase for the second harmonic, which is therefore enhanced. As a result, we change the period of the final oscillation through our coherent control so as to synthesize our waveform.

3. Applications

3.1. Nanoultrasonic imaging

Picosecond ultrasonics, by using a metallic layer as a transducer, has been the most advanced tool to achieve images with a longitudinal spatial resolution of tens of nanometer [42]. By using CAP generated by nitride based piezoelectric heterostructures, we have successfully performed a one-dimensional ultrasonic-scan measurement, in which a longitudinal resolution better than $\lambda/16$, corresponding to sub-nanometer resolution, was achieved [4]. Using

this technique, we were recently able to study the organization of water at the interface with a hydrophilic solid with a sub-nanometer molecular resolution [43]. Though the longitudinal resolution is down to sub-nanometers, the lateral resolution is still limited to the vast optical spot size, which is of the order of micrometers. In order to improve the lateral resolution for a real three-dimensional (3D) nanoultrasonic imaging application, we have proposed and demonstrated a novel method, called force-saturation technique, to spatially manipulate the carrier distribution and thereby the phonon driving force in piezoelectric heterostructure. A drastic improvement on lateral resolution from tens of micrometers down to 100 nm was then achieved, sufficiently below the diffraction limit of the optical spot size [44]. Taking advantage of the force-saturation technique, we have further realized a 3D subsurface characterization, in which experiment a thin nanolayer of SiO_2 deposited on a patterned GaN epitaxial layer was successfully imaged [45]. It is worth noting that in addition to the force-saturation technique for CAP excitation, the oversampling technique during B-scan as well as the post imaging processing technique of deconvolution could further promote the lateral resolution that can be even better
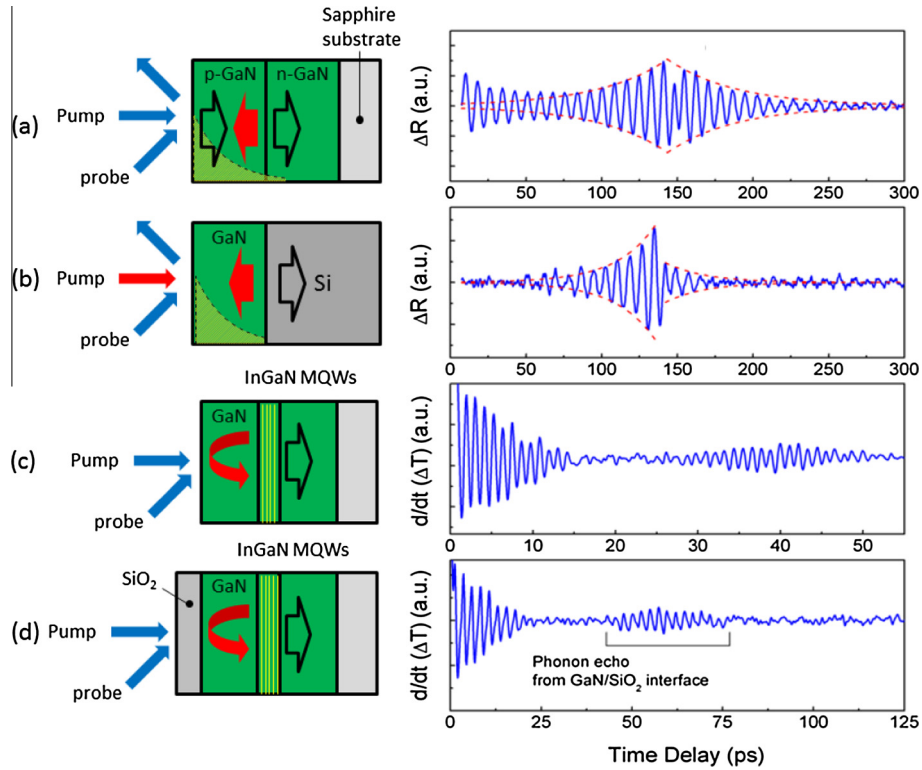
Fig. 11. (a) and (b) Extracted transient optical reflectivity (solid lines) measured with a GaN p–n junction and a GaN = Si epilayer. The concerned features of phonon reflection are depicted as dashed lines. (c) and (d) Differential transient transmission changes obtained in a 14-period InGaN/GaN MQW and a 10-period InGaN/GaN MQW with a SiO$_2$ cap layer (adapted from Ref. [46]).

than 50 nm, as previously compared to that by atomic force microscopy [45]. That is, the nitride based piezoelectric heterostructures with appropriate excitation and sampling techniques have been demonstrated to be an excellent THz coherent acoustic phonon source for 3D nanoultrasonics.

3.2. Roughness measurements

Thanks to the demonstration of the high longitudinal resolution, nanoultrasonics has the potential to image [43] or even probe sub-nanoscale structures. We also applied similar principles to measure interface roughness [46]. For nanoultrasonic imaging applications, subsurface interfacial roughness has played a crucial role in the specular scattering of *coherent* acoustic phonons because the wavelengths of sub-THz/THz acoustic phonon are comparable to the roughness. We have quantitatively investigated the specular scattering probability (SSP) by monitoring the phonon reflection behaviors at different air/GaN interfaces, where the GaN surface morphology could be well manipulated [46]. In our experiment, the surface roughness was controlled from 0.2 to ~10 nm. Fig. 11 shows the schematic diagrams of our adopted sample structures and the corresponding differential optical pump–probe traces.

In the first two cases, acoustic phonons were initiated from a p–n junction in a GaN epi-structure and a Si substrate, respectively. By measuring the amplitude drop of coherent acoustic phonons at the interface, the SSP thus could be estimated. In the third case, we have adopted MQWs to generate 890 GHz acoustic phonons, which correspond to the main phonon when temperature is down to 10 K [47]. In this case, the acoustic phonon attenuation due to anharmonic coupling, which will be discussed later, should be well calibrated before estimating the SSP [46]. Fig. 12 shows the measured SSP as a function of roughness, after the calibration procedure.
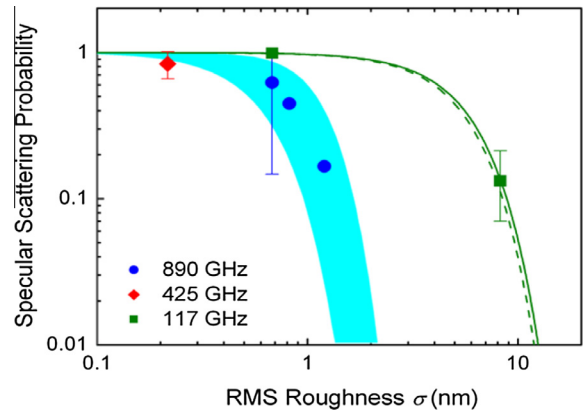
Fig. 12. Specular scattering probability (SSP) as a function of σ measured in four samples (dots). The 890 GHz data were obtained on different locations of a specific sample, while the other low-frequency data were taken from different samples. The solid (dashed) line depicts the SSA prediction for the scatterings of 117 GHz phonons at the GaN p–n junction (GaN/Si) sample surface, while the same theoretical investigation for 890 GHz phonons is represented by the ranged area due to uncertainty in correlation lengths (adapted from Ref. [47]).

One notices that the 117 GHz CAP (green square) reflected from a flat interface (root-mean-square roughness $\sigma = 0.62$ nm) experienced almost no losses, while the same CAP reflected from a rough interface ($\sigma \sim 8.2$ nm) was severely attenuated. For high-frequency measurement, the SSP were even more sensitive to the surface roughness. For example, we found that the measured SSP for 890 GHz acoustic phonons had dropped from 0.62 to 0.17 when the roughness was increased from 0.68 to 1.2 nm. This result indicated that high-frequency acoustic phonons were more vulnerable to atomic-scaled roughness. Based on these preliminary

results, we have further elucidated the dominant role of surface irregularity by measuring the reflection of 425 GHz acoustic phonons at an atomically flat but buried GaN/SiO$_2$ interface ($\sigma \sim 0.2$ nm), which was confirmed by transmission electron microscopy. As estimated by a slow slope approximation model (SSA), this low roughness should yield a low diffusive scattering (or SSP >0.8) [48,49]. As a result, the measured SSP at this perfect GaN/SiO$_2$ interface for 425 GHz phonons was 0.83. The reasonable agreement between the experiment and the roughness-based scattering theory indicates that CAP can not only provide high resolution imaging, but also provide accurate estimation for interface roughness with an angstrom level accuracy.

3.3. THz hypersound attenuation spectra in solids

THz phonon spectroscopy, as we have seen, has the potential not only to perform high resolution imaging of embedded structures [45], but also to probe their mechanical, elastic and thermal characteristics. However, one of the main drawbacks of THz phonon is their strong attenuation. Multiple mechanisms, from lattice imperfections, doping concentration, to anharmonic coupling, are responsible for the strong attenuation that THz phonons suffer [50]. The understanding of these THz acoustic phonon transport, loss, and scattering mechanisms is critical for thermal management in future nano-sized 0D to 3D devices and electrical circuits. In the following, we discuss our THz bandwidth THz hypersound measurement on the effect of the lattice imperfections and anharmonic coupling on phonon scatterings for sub-THz/THz acoustic waves.

3.3.1. Threading dislocation in GaN

In theory, phonon lifetime due to dislocation scatterings can be expressed as $\tau_{dislocations}^{-1} = C_1 N_d b^2 \omega$, where N_d is the number of

dislocation lines per unit area, b is the magnitude of Burger's, ω is the phonon frequency, and C_1 is the proportionality constant that depends on the type of dislocation [37]. In order to characterize the structural defect effects, we have performed nanoultrasonic measurement on a GaN light emitting diode (LED) structure, in which the threading dislocations were artificially formed. The sample was grown on a wet-etched strip-patterned sapphire substrate. By using the photolithography and regrowth technique, we have synthesized a GaN:Si buffer layer, where area with a high- and a low-dislocation-density, 10^6 cm^{-2} and 10^8 cm^{-2}, respectively, were periodically distributed. More details on the sample can be found elsewhere [51,52]. In the experiment, we observed that the coherent acoustic waves (Brillouin oscillations) were attenuated accordingly to the density of the threading dislocations. Fig. 13 shows the measurement results and a schematic representation of the sample.

The measured Brillouin oscillations had a period of approximately 10 ps, corresponding to a phonon frequency of 100 GHz in the GaN:Si layer. In Fig. 13(a), we observed an exponential decay (dotted curve), with a decay time of approximately 200 ps, of the phonon amplitude in the high-density zone. Then, the focal spot was moved to the low-density region, where the dislocation density was reduced by a factor of 100. By assuming the same homogenous Burger's vectors and C_1 for this position, the phonon lifetime was estimated to be 20 ns. As expected, the pump–probe trace shows almost no decay during the initial 150 ps, as can be seen in Fig. 13(b). Taking the sound velocity of ~8000 m/s in GaN:Si, the traveling depth is calculated to be 1.23 μm below the surface of sample. Thereafter, a decay was observed between 150 and 400 ps, and no further decrease after 400 ps. This result indicated that there existed a high-dislocation-density region between the depths of 1.23 and 3.28 μm, and at depths deeper than 3.28 μm, there was a recovery and the dislocation density was low. This result agrees with the fact that even though most of the threading
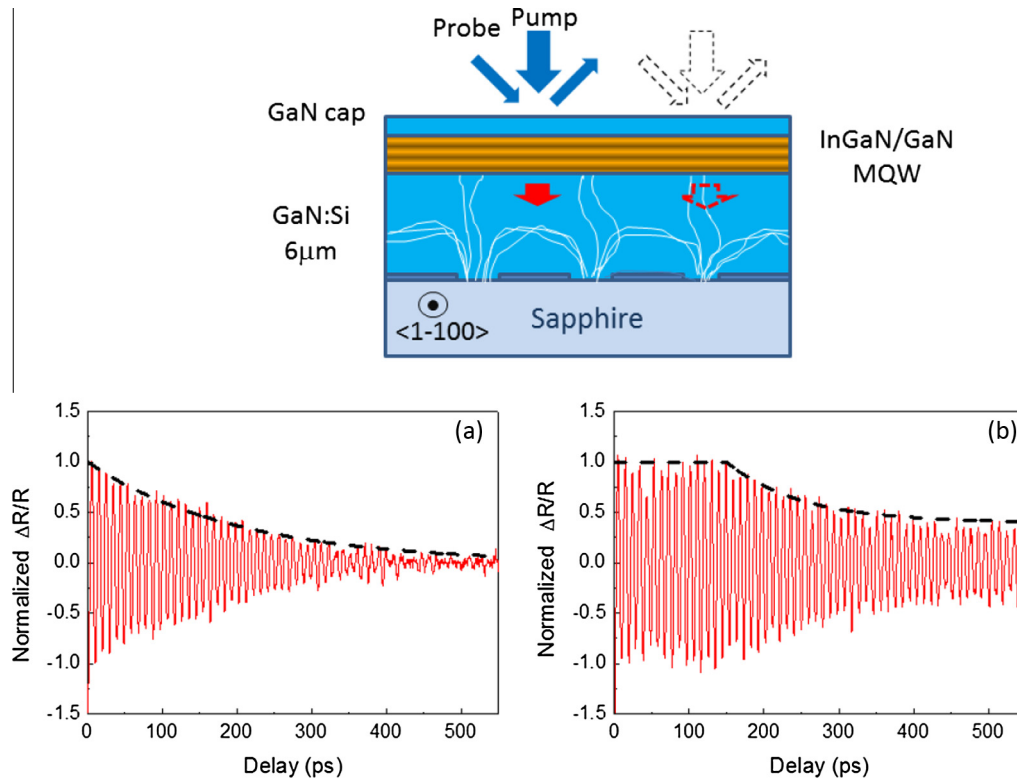
Fig. 13. Measured differential reflections as a function of time delay at (a) high and (b) low dislocation density area. The dotted curve in (a) is the curve used for fitting the lifetime of nano-acoustic waves, and it shows a 200-ps exponential decay. The inset shows the schematic diagram of the sample with periodically distributed high and low dislocation density areas (adapted from Ref. [52]).

dislocations are guided and suppressed in a region close to the sapphire interface, there were still inevitably a non-negligible number of threading dislocations stretching laterally in the middle of the GaN:Si layer. In conclusion, nanoultrasonics was demonstrated not only capable of estimating dislocation densities but also capable of imaging the dislocation distributions.

3.3.2. Anharmonic coupling in crystalline GaN: the Herring effect

High-frequency (>300 GHz) acoustics waves are especially suitable for the investigation of anharmonic coupling. Traditionally the acoustic phonons are subthermal ($\hbar\omega \ll KT$) and the angular frequency ω is much slower than the thermal phonon lifetime τ_{th} in materials, i.e., $\omega\tau_{th} \ll 1$. Therefore, acoustic attenuation due to crystal anharmonicity can be adequately described by macroscopic relaxation damping with a linear temperature dependency [53]. However, the frequency of optically initiated acoustic waves in nanoultrasonics is so high that $\omega\tau_{th}$ could be much greater than 1 [54]. Under such a condition, the attenuation caused by relaxation damping will be independent of phonon frequency [52]. Quantum mechanical three-phonon scattering processes, other than macroscopic relaxation damping, will emerge to play an important role in the anharmonic decay. This situation has been considered theoretically in Herring's early work [55]. In the theory, the frequency of acoustic phonons should be lower than that of thermal phonons ($\omega \ll KT/\hbar$) but high enough to satisfy the criterion of $\omega\tau_{th} \geqslant 1$, from which the acoustic attenuation is derived to be proportional to $\omega^2 T^3$ in C_{6v} symmetry of wurtzite GaN at temperatures much lower than the Debye temperature [55]. To experimentally validate the process, we have to exploit our developed technique to study the anharmonic decay of acoustic phonons with a frequency in the subterahertz range [56]. Consider 4.8 ps for the thermal phonon lifetime in GaN [56], we confirmed that the product of our adopted acoustic phonon frequency and thermal phonon lifetime is 14.17, satisfactorily much higher than 1. In this work, we have first performed femtosecond pump–probe measurement on two MQW samples, which generated and detected coherent acoustic phonons with 380 and 470 GHz as their fundamental frequencies, respectively. By changing the sample temperature from 80 K to room temperature, we eliminated the collision rate $\tau_{dislocations}^{-1}$ from lattice imperfections, which shall be temperature independent, and extracted the phonon lifetime τ_{anh} caused by anharmonicity. It is noted that even at the lowest measured temperature (80 K), the acoustic phonon frequency (470 GHz) is still much lower than the dominant thermal phonons ($KT/\hbar$ = 1.67 THz). That is to say, the experiment by using subteraherz acoustic waves was perfectly suitable for investigating for the first time whether the Herring proposed process should be responsible for the anharmonic decay in GaN crystals. Fig. 14 shows the experimental result of the measured time constant as a function of the sample temperature T.

To elucidate the process responsible for the measured decay time constant, we fitted the anharmonic decay rate τ_{anh}^{-1} by $c\omega^a T^b$ with the least sum of squared error for two frequencies. The fitted value b is 3.2 ± 0.12 for the 470 GHz case and 3.06 ± 0.03 for the 380 GHz case (both are within an acceptable range of error), implying a cubic dependence of τ_{anh}^{-1} on the crystal temperature. When the parameter b is set as 3.08, which is acceptable for both cases, the frequency dependence a is 1.98 ± 0.27. In brief, the τ_{anh}^{-1} of longitudinal acoustic phonons in wurtzite GaN show $\sim\omega^a T^b$ dependence. This trend satisfactorily agreed with Herring's derivation for the C_{6v} symmetry of wurtzite GaN at temperatures much lower than the Debye temperature [55]. Even though the attenuation at this frequency is well described by Herring's process in GaN, as the temperature and frequency dependence demonstrate it, multiple phenomena are responsible for the observed attenuation. Among them, the sample defects and imperfections can play a dominant role. We therefore grow a high quality GaN layer sandwiched by two MQWs structures as depicted in Fig. 15(a). Both pump and probe beam are incident from the top side of the sample. The obtained transient transmission changes trace is reproduced in Fig. 15(b). Multiple contributions are observed. At the beginning of the signal the detection of the acoustic strain by the MQWs is observed. Then after propagation in the sample, multiple echoes, called 2, 3 and 4 are detected. The path of each contribution is depicted in Fig. 15(a). By taken into account the measured pump transmission in both MQWs, which is 0.96, the acoustic signals generated and detected in MQW B should be weaker than those in MQW A by 96%. Therefore, the strength of echo 4 should be calibrated by dividing this value. Fig. 15(c) shows the power spectrum of echo 2 and echo 4 after normalization. It indicates that during the propagation in the 2 μm layer, the energy of the acoustic wave at 435 GHz slightly decreases. The attenuation at this frequency can then be calculated using the following equation:

$$\alpha(\omega) = \frac{1}{d_s} \ln\left[\frac{\Delta R_1(\omega)}{\Delta R_2(\omega)}\right] \tag{15}$$

where d_s is the traveling distance, R_1 and R_2 are the peak value of the power spectrum of the second and fourth echoes respectively. Based on the above equation, the attenuation at 435 GHz is found to be 0.026 μm^{-1}, which corresponds to a phonon lifetime of 4.80 ns. With this result, the coefficient c can be determined to be less than 1.03×10^{-24}. It is important to note that our measured lifetime shows the lower bound for real acoustic phonon lifetime. Indeed, experimentally we measured the attenuation constant not only due to anharmonic effects, but also, as we mentioned previously, imperfections, therefore the phonon lifetime can be even longer in an even-better-quality sample.
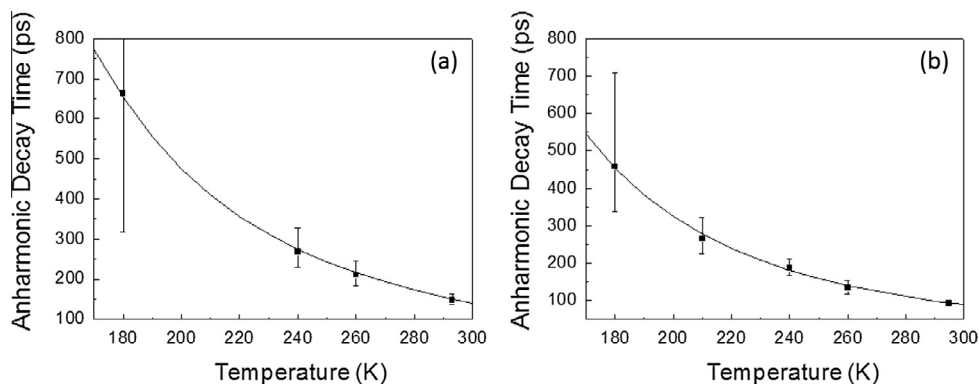
Fig. 14. Measured decay time (solid squares) of 470 and 380 GHz longitudinal coherent acoustic phonons propagating in GaN at different temperatures. Error bars represent the standard deviation of measured values. The fitted curves show an inverse cubic dependence on temperature (adapted from Ref. [56]).
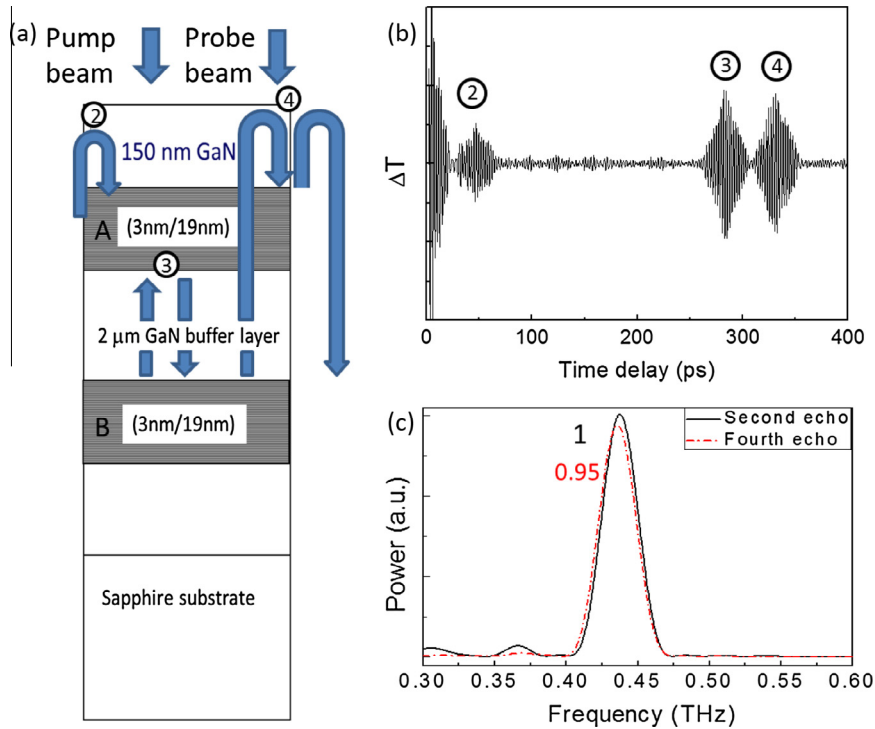
Fig. 15. (a) The schematic of our sample structure and paths of generated acoustic waves. (b) The measured result by the femtosecond pump–probe system. (c) The power spectra of the echo 2 and echo 4. The difference is due to propagation in a 2 μm-thick GaN layer.

3.3.3. Phonon attenuation spectra in vitreous silica by broadband nanoultrasonic spectroscopy

Apart from the single crystalline GaN, we have also performed the nanoultrasonic spectroscopic measurement on a vitreous SiO$_2$ (v-SiO$_2$) thin film. In the experiment, we have utilized a 3 nm InGaN/GaN SQW layer to generate and detect an ultra-short ($\sim$730 fs) strain pulse, corresponding to an acoustic bandwidth up to 1.3 THz [14]. By analyzing the strain echoes reflected from GaN/v-SiO$_2$ and v-SiO$_2$/air interfaces, we extended the hypersound attenuation measurement in v-SiO$_2$ up to 650 GHz, which had never been reached before in the same system [57–59]. Recently, Lin et al. have further extended the frequency up to 740 GHz by measuring the second harmonic phonon signal generated from a MQW structure [60]. Fig. 16 shows the measured linewidth $\Gamma/2\pi$,
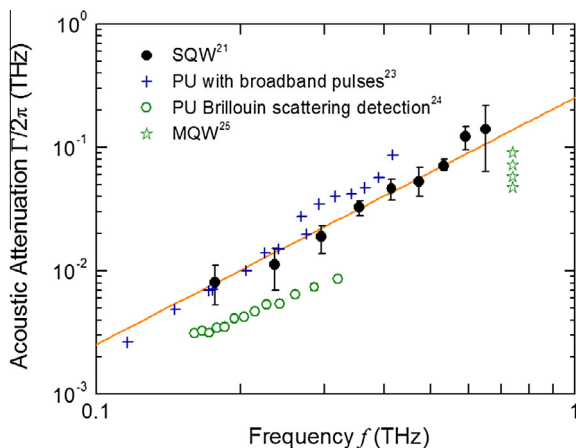
which is converted from the attenuation coefficient α and sound velocity c by $\Gamma = \alpha c$.

In Fig. 16, our measured data points are shown in solid circles. Several other works were also included for comparisons. It should be noted that the SSP at the interfaces has also been taken into account to retrieve the accurate hypersound attenuation coefficients. In the frequency range of 180–650 GHz, our data showed a clear $\Gamma \propto f^2$ behavior, suggesting that the damping mechanism for hypersounds is anharmonicity. According to the X-ray scattering experiment ($f > 1$ THz) [61] and the observed plateau in thermal conductivity of glasses around 10 K [62], it is expected that Γ should transit from f^2 to f^4 regime at a frequency less than the Ioffe-Regel limit ($\sim$1 THz). Without observing this transition at $f < 0.7$ THz, however, our ultrasonic data thus implies that the high-order damping process ($\Gamma \propto f^4$), caused by the interaction with quasilocal vibration and/or phonon scattering by frozen-in disorder [47], could become predominant in an even higher frequency range, i.e., 0.7–1 THz.

3.3.4. THz broadband attenuation by measurements of complex acoustic impedance at high frequency

Measuring the attenuation at high frequency is, as we have seen, critical to understand thermal properties of materials. However, it becomes increasingly more difficult to perform these measurements since attenuation becomes much severe at high frequency. A possibility to overcome this limitation is to perform attenuation measurements in thinner layer, typically on the order of 10 nm. But this method creates new issues, such as modifications of the layer properties due to confinement.

We recently demonstrated a new method enabling the broadband measurement of hypersound attenuation up to the record frequency of 1 THz in any materials [63]. The principle of this technique is quite simple: when the frequency of acoustic phonons becomes high, they are strongly attenuated, but consequently the imaginary part of the complex acoustic impedance cannot be neglected anymore. In that case, the impedance is given by:

Fig. 16. Acoustic attenuation coefficient of v-SiO$_2$. Data from previous picosecond ultrasonic (PU) and multiple quantum well (MQW) measurements are also shown for comparison. The thin line with a slope of 2 is a guide for eye (adapted from Ref. [60]).

$$Z(\omega) = \rho \frac{\omega}{k(\omega) + i\alpha(\omega)} \qquad (16)$$

where ω is the frequency, ρ is the mass density, k is the acoustic wavenumber and α, the attenuation constant. At low frequency, the attenuation is negligible and thus, the impedance is the product of the density by the sound velocity. However, when the frequency increases, the attenuation modifies the acoustic impedance and thus the reflection at interfaces. It then becomes possible to measure the attenuation constant of a material, without propagating within this material, allowing the measurement at extremely high frequency. The idea of the experiment is to grow a layer of a material to be characterized on top of the sample, and study the acoustic reflection at the interface between the sample and the material to be characterized as a function of the frequency. However, it is possible to greatly improve the quality and reliability of the measurement by performing experiments *in-situ*.

We realized a demonstration of this principle by studying the attenuation spectrum of ice, up to 1 THz, with either a SQW or a MQW embedded structure. We first placed the samples in a cryogenic system and performed nanoultrasonic experiments at 150 K under low pressure. We thus obtained the reflection from the GaN/vacuum interface. We then grow ice within the chamber by increasing the pressure while keeping the temperature at 150 K. Another experiment is then performed and the reflection of the GaN/ice interface is obtained. By doing the ratio between the two reflections, we are able to remove some undesired contributions from the reflection coefficient of the GaN/ice interface. For example, with this method, the losses due to propagation or roughness scattering are suppressed. But this method also allows us to not only retrieve the amplitude of the reflection, but also the phase. With these two pieces of information, we can calculate the attenuation constant of ice using Eq. (16), as shown in Fig. 17.

One remarks that at low frequencies, the attenuation constant follows a frequency-squared dependency, typical of damping due to interaction with the thermal phonon bath. However at higher frequency, a saturation of the absorption is observed. Indeed, at this frequency, we have $\omega\tau > 1$, with τ the thermal phonon lifetime, which means that the thermal phonon bath doesnot have time to interact with the acoustic phonon. Thanks to this saturation we were able to get an estimation of the thermal phonon lifetime of ice at 150 K, $\tau = 0.2$ ps.

In summary, we have not only investigated the lattice imperfections in the GaN LED samples, but also the anharmonic coupling for sub-THz acoustic phonons in both crystalline GaN and vitreous SiO_2 by using the ultra-broadband THz OPTs. The nanoacoustic waves in semiconductors are not only capable of imaging the subsurface nano-morphology, but also capable of imaging the structural defects for important electronic nano-devices. Taking advantage of the MQW structures, we also found that the interactions between sub-THz (380 and 470 GHz) acoustic and thermal phonons should be accounted for by quantum mechanical three-phonon scattering processes. Finally, by using a piezoelectric nanolayer, an ultrashort strain pulse provide us with unprecedented acoustic bandwidth from 0.18 to 1.3 THz, which thus allows us to bridge the spectral gap (0.1–1 THz) between inelastic light and X-ray scatterings for the study of lattice dynamics. Taking $\omega\tau_{th}$ as a critical number, we have examined the THz hypersound attenuation spectra in materials with $\omega\tau_{th} \ll 1$, ~ 1, and $\gg 1$. These regimes correspond to our above discussed measurements in vitreous SiO_2, ice, and crystalline GaN.
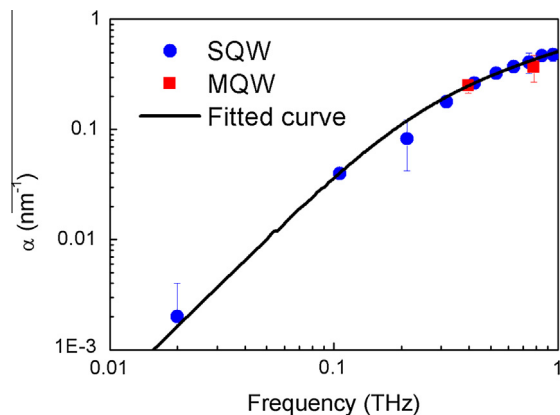
3.4. Phononic bandgap nanocrystal characterization and superluminal paradox

Taking advantage of the broadband CAP generated by a SQW, the study of the frequency dependent behavior of different structures can be studied. For example, we have experimentally investigated the transient characteristic of a phononic bandgap nano-crystal [64]. By constructing a THz LA phonon cavity, we have experimentally obtained the transfer function of a 17 period MQW structure with barrier and well width of 8 nm, acting as a phononic bandgap nano-crystal (PhonBC) with first frequency gap centered at 0.28 THz. The amplitude and phase of the reflectivity of the PhonBC are reproduced in Fig. 18.

We observe that the frequencies located close to 0.28 THz are more reflected, revealing the phonon stop band of the phonBC. Moreover, a good agreement is observed between our experimental observation (solid circles) and theoretical predictions (solid lines) [65].

From the experimentally obtained phase information and the directly measured reflected waveform in time domain, we can further investigate interesting phononic bandgap phenomena, which
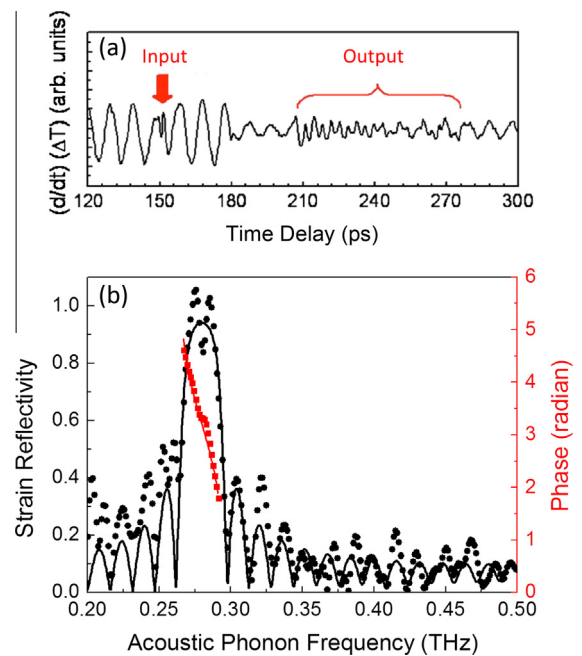
Fig. 18. (a) Transient transmission change exhibiting the waveform of the generated CAP (Input) and the waveform reflected by the phonBC. (b) Experimentally obtained amplitude (dots) and phase (triangles) spectra of the reflection transfer function of the nanoacoustic mirror with superlattice structure. The theoretical amplitude (thick solid line) and phase (thin solid line) spectra are obtained by the transfer matrix method.

Fig. 17. THz hypersound spectrum showing the attenuation coefficient of ice measured by the complex acoustic impedance technique.
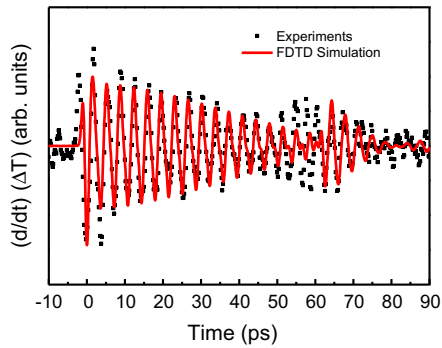
Fig. 19. Experimental trace and FDTD simulation of the waveform of the reflection of a Gaussian acoustic wavepacket by the PhonBC. A good agreement is obtained, and a round trip time of 60 ps is observed, demonstrating that there is no supersonic transport, as might be calculated by the "phase time."

can be compared with the previously debated photonic bandgap issues [66–68]. Winful has proposed that a broadband optical wavepacket can propagate into the photonic bandgap crystal while a narrowband optical wavepacket do not [66]. It is thus interesting to investigate whether the bandgap photons or acoustic phonons inside an ultrashort, or ultra-broadband, wavepacket propagate into the photonic or phononic bandgap crystal. Here, we have generated LA phonon wavepacket with a pulse width shorter than the length of the phonon barrier.

First, we may describe the time delay of the bandgap LA phonons upon reflection by using the phase slope ($-d\phi/d\omega$) in the transfer function represented as $|T(\omega)|e^{i\phi}$. Thus retrieved time delay, called phase time, of 16.4 ps can be obtained from our experimentally recovered transfer function as shown in Fig. 18. Previous studies revealed that this value described the time delay of the reflected or tunneled ultra-narrowband pulses [66]. However, for ultra-broadband pulses, it is difficult to understand the physical meaning of ($-d\phi/d\omega$) to describe the much lengthened reflected waveform, the measured reflected waveform being seriously distorted compared with the incident Gaussian-like wavepacket.

To understand the reflected bandgap LA phonon waveform, it should be noted that a PhonBC becomes a phonon barrier when the standing waves exist inside it. Since the pulse width of the incident wavepacket here is much shorter than the phonon barrier length, what we observed is the transient forming process of standing waves inside the PhonBC. Our experimentally obtained reflected LA phonon wavepacket with lengthened shape as shown in Fig. 18, infers that the bandgap LA phonons propagate inside the PhonBC, and bounce back and forth with attenuation. To further verify the propagating dynamics of the bandgap LA phonons inside the PhonBC, we can use a finite-difference-time-domain method to simulate the evolution of the strain distribution as depicted in Fig. 19 (red[1] solid line).

When the ultrashort LA phonon wavepacket enters into the PhonBC, it travels with LA velocity in each layer without much distortion since most of the acoustic frequencies lie on the transmission band. Nevertheless, the bandgap LA phonons bounce back and forth inside the PhonBC, resulting in transiently formed standing waves. Using this FDTD method, we can thus compared the experimental signal (black dots) to the simulated waveform (red solid line), as in Fig. 19.

We can observe a good agreement between these two traces. One remarks that in both cases, we observe an enhanced signal around 60 ps, which corresponds to the round-trip inside the PhonBC at the group velocity. In the case of ultra-narrow band

pulses, they determined the time to travel through a barrier to be equal to the phase time, thus speculating on possible superluminal transport [69]. Our results confirms Winful's predictions that phase time is not necessarily the energy transmission time, and that photons, or phonons, travel at the group velocity in a barrier [65]. Our results also reveal that the bandgap LA phonons are not considered quantum–mechanically as forbidden in the PhonBC with a finite thickness.

4. Conclusion

We have shown that nitride semiconductor heterostructures are able, thanks to the built in piezoelectric field, to generate broadband or monochromatic CAP with frequencies in the sub-THz to >2.4 THz range. Thanks to the generation mechanism, the direct generation of CAP with different polarizations and methods to realize pulse shaping have been demonstrated. Thanks to the broad spectrum and the record-high frequency of the CAP generated by nitride based semiconductor heterostructures, acoustic imaging with unparalleled resolution and, measurements of sound attenuation at extremely high frequency can thus be achieved for the first time.

References

[1] C. Thomsen, J. Strait, Z. Vardeny, H.J. Maris, J. Tauc, J.J. Hauser, Phys. Rev. Lett. 53 (1984) 989.
[2] C. Thomsen, H.T. Grahn, H.J. Maris, J. Tauc, Phys. Rev. B 34 (1986) 4129.
[3] O.B. Wright, J. Appl. Phys. 71 (1992) 1617.
[4] K.-H. Lin, G.-W. Chern, C.-T. Yu, T.-M. Liu, C.-C. Pan, G.-T. Chen, J.-I. Chyi, S.-W. Huang, P.-C. Li, C.-K. Sun, IEEE Trans. Ultrason. Ferroelectr. 52 (2005) 1404.
[5] H.N. Lin, R.J. Stoner, H.J. Maris, J. Tauc, J. Appl. Phys. 69 (1991) 3816.
[6] J.-Y. Duquesne, B. Perrin, Phys. Rev. B 68 (2003) 134205.
[7] T. Saito, O. Matsuda, O.B. Wright, Phys. Rev. B 67 (2003) 205421.
[8] Y.-C. Wen, G.-W. Chern, K.-H. Lin, J.-J. Yeh, C.-K. Sun, Phys Rev. B 84 (2011) 205315.
[9] P.-A. Mante, A. Devos, A. Le Louarn, Phys. Rev. B 81 (2010) 113305.
[10] G.-W. Chern, K.-H. Lin, C.-K. Sun, J. Appl. Phys. 95 (2004) 1114.
[11] O. Matsuda, O.B. Wright, D.H. Hurley, V.E. Gusev, K. Shimizu, Phys. Rev. Lett. 93 (2004) 095501.
[12] Y.-C. Wen, L.-C. Chou, H.-H. Lin, V. Gusev, K.-H. Lin, C.-K. Sun, Appl. Phys. Lett. 90 (2007) 172102.
[13] P. Babilotte, P. Ruello, G. Vaudel, T. Pezeril, D. Mounier, J.-M. Breteau, V. Gusev, Appl. Phys. Lett. 97 (2010) 174103.
[14] Y.-C. Wen, S.-H. Guol, H.-P. Chen, J.-K. Sheu, C.-K. Sun, Appl. Phys. Lett. 99 (2011) 051913.
[15] G.-W. Chern, C.-K. Sun, G.D. Sanders, C.J. Stanton, in: K.-T. Tsen (Ed.), Ultrafast Dynamical Processes in Semiconductors, Springer, Berlin/Heidelberg, 2004.
[16] G.D. Sanders, C.J. Stanton, C.S. Kim, Phys. Rev. B 64 (2001) 235316.
[17] Chi-Kuang Sun, Jian-Chin Liang, Christopher J. Stanton, Amber Abare, Larry Coldren, Steven P. DenBaars, Appl. Phys. Lett. 75 (1999) 1249.
[18] C.-K. Sun, J.-C. Liang, X.-Y. Yu, Phys. Rev. Lett. 84 (2000) 179.
[19] A.A. Maznev, K.J. Manke, K.-H. Lin, K.A. Nelson, C.-K. Sun, J.-I. Chyi, Ultrasonics 52 (2012) 1.
[20] C. Deger, E. Born, H. Angerer, O. Ambacher, M. Stutzmann, J. Hornsteiner, E. Riha, G. Fischerauer, Appl. Phys. Lett. 72 (1998) 2400.
[21] A. Polian, M. Grimsditch, I. Grzegory, J. Appl. Phys. 79 (1996) 3343–3344.
[22] Chien-Cheng Chen, Huei-Min Huang, Lu Tien-Chang, Hao-Chung Kuo, Chi-Kuang Sun, Appl. Phys. Lett. 100 (2012) 201905.
[23] Y.-C. Wen, T.-S. Ko, T.-C. Lu, H.-C. Kuo, J.-I. Chyi, C.-K. Sun, Phys. Rev. B 80 (2009) 195201.
[24] A.M. Weiner, D.E. Leaird, G.P. Wiederrecht, K.A. Nelson, Science 247 (1990) 1317.
[25] W.S. Warren, H. Rabitz, M. Dahleh, Science 259 (1993) 1581.
[26] N.H. Bonadeo, J. Erland, D. Gammon, D. Park, D.S. Katzer, D.G. Steel, Science 282 (1998) 1473.
[27] M.U. Wehner, M.H. Ulm, D.S. Chemla, M. Wegner, Phys. Rev. Lett. 80 (1998) 1992.
[28] R. Atanasov, A. Haché, J.L.P. Hughes, H.M. van Driel, J.E. Sipe, Phys. Rev. Lett. 76 (1996) 1703.
[29] A. Bartels, T. Dekorsy, H. Kurz, K. Ko, Appl. Phys. Lett. 72 (1998) 2844–2846.
[30] N.-W. Pu, J. Bokor, S. Jeong, R.-A. Zhao, Appl. Phys. Lett. 74 (1999) 115428.
[31] A. Arbouet, N. Del Fatti, F. Vallee, J. Chem. Phys. 124 (2006) 144701.
[32] T. Pezeril, C. Klieber, S. Andrieu, K.A. Nelson, Phys. Rev. Lett. 102 (2009) 107402.
[33] N.D. Lanzillotti-Kimura et al., Phys. Rev. B 84 (2011) 115453.
[34] C.-K. Sun, Y.-K. Huang, J.-C. Liang, A. Abare, S.P. DenBaars, Appl. Phys. Lett. 78 (2001) 1201.

---

[1] For interpretation of color in Fig. 19, the reader is referred to the web version of this article.

[35] C.-K. Sun, G.-W. Chern, K.-H. Lin, Y.-K. Huang, Chinese J. Phys. 41 (2003) 643–651.
[36] C.-L. Hsieh, K.-H. Lin, S.-B. Wu, C.-C. Pan, J.-I. Chyi, C.-K. Sun, Appl. Phys. Lett. 85 (2004) 4735.
[37] A.V. Akimov, A.V. Scherbakov, D.R. Yakovlev, C.T. Foxon, M. Bayer, Phys. Rev. Lett. 97 (2006) 037401.
[38] J.M. Dela Cruz, I. Pastirk, M. Comstock, V.V. Lozovoy, M. Dantus, Proc. Natl. Acad. Sci. USA 101 (2004) 16996.
[39] W. Maryam, A.V. Akimov, R.P. Campion, A.J. Kent, Nature Commun. 4 (2013) 2184.
[40] C.-T. Yu, K.-H. Lin, C.-L. Hsieh, C.-C. Pan, J.-I. Chyi, C.-K. Sun, Appl. Phys. Lett. 87 (2005) 093114.
[41] G.-W. Chern, K.-H. Lin, Y.-K. Huang, C.-K. Sun, Phys. Rev. B 67 (2003) 121303.
[42] H.T. Grahn, H.J. Maris, J. Tauc, Picosecond ultrasonics, IEEE J. Quantum Electron. 25 (1989) 2562–2569.
[43] P.-A. Mante, C.-C. Chen, Y.-C. Wen, H.-Y. Chen, S.-C. Yang, Y.-R. Huang, I.-J. Chen, Y, -W. Chen, V. Gusev, M.-J. Chen, J.-L. Kuo, J.-K. Sheu, C.-K. Sun, Sci. Rep. 4 (2014) 6249.
[44] K.-H. Lin, C.-M. Lai, C.-C. Pan, J.-I. Chyi, J.-W. Shi, S.-Z. Sun, C.-F. Chang, C.-K. Sun, Nat. Nanotechnol. 2 (2007) 704–708.
[45] K.-H. Lin, C.-T. Yu, S.-Z. Sun, H.-P. Chen, C.-C. Pan, J.-I. Chyi, S.-W. Huang, P.-C. Li, C.-K. Sun, Appl. Phys. Lett. 89 (2006) 043106.
[46] Y.-C. Wen, C.-L. Hsieh, K.-H. Lin, S.-B. Wu, S.-C. Chin, C.-L. Hsiao, Y.-T. Lin, C.-S. Chang, Y.-C. Chang, L.-W. Tu, C.-K. Sun, Phys. Rev. Lett. 103 (2009) 264301.
[47] E.T. Swartz, R.O. Pohl, Rev. Mod. Phys. 61 (1989) 605.
[48] S.L. Broschat, E.I. Thorsos, J. Acoust. Soc. Am. 101 (1997) 2615.
[49] S.L. Broschat, IEEE Trans. Geosci. Remote Sens. 37 (1999) 632.
[50] P.G. Klemens, Proc. Phys. Soc. A 68 (1955) 1113.
[51] C.-C. Pan, C.-H. Hsieh, C.-W. Lin, J.-I. Chyi, J. Appl. Phys. 102 (2007) 084503.
[52] T.-M. Liu, S.-Z. Sun, C.-F. Chang, G.-T. Chen, C.-C. Pan, J.-I. Chyi, C.-K. Sun, Chinese J. Phys. 49 (1) (2011) 171–175.
[53] H.J. Maris, in: W.P. Mason, R.N. Thurston (Eds.), Physical Acoustics, vol. 8, Academic, New York, 1971, p. 279.
[54] B.W. Chen, H.J. Maris, Z.R. Wasilewski, S. Tamura, Philos. Mag. B 70 (1994) 687.
[55] C. Herring, Phys. Rev. 95 (1954) 954.
[56] T.-M. Liu, S.-Z. Sun, C.-F. Chang, C.-C. Pan, G.-T. Chen, J.-I. Chyi, V. Gusev, C.-K. Sun, Appl. Phys. Lett. 90 (2007) 041902.
[57] E. Pontecorvo, M. Ortolani, D. Polli, M. Ferretti, G. Ruocco, G. Cerullo, T. Scopigno, Appl. Phys. Lett. 98 (2011) 011901.
[58] T.C. Zhu, H.J. Maris, J. Tauc, Phys. Rev. B 44 (1991) 4281.
[59] A. Devos, M. Foret, S. Ayrinhac, P. Emery, B. Ruffle, Phys. Rev. B 77 (2008) 100201.
[60] K.-H. Lin, D.-H. Tsai, K.-J. Wang, S.-H. Chen, K.-L. Chi, J.-W. Shi, P.-C. Chen, J.-K. Sheu, AIP Adv. 3 (2013) 072126.
[61] G. Baldi, V.M. Giordano, G. Monaco, B. Ruta, Phys. Rev. Lett. 104 (2010) 195501.
[62] T. Nakayama, Rep. Prog. Phys. 65 (2002) 1195.
[63] P.-A. Mante, C.-C. Chen, Y.-C. Wen, J.-K. Sheu, C.-K. Sun, Phys. Rev. Lett. 111 (2013) 225901.
[64] K.-H. Lin, C.-F. Chang, C.-C. Pan, J.-I. Chyi, S. Keller, U. Mishra, S.P. DenBaars, C.-K. Sun, Appl. Phys. Lett. 89 (2006) 143103.
[65] S. Mizuno, S. Tamura, Phys. Rev. B 45 (1992) 734.
[66] H. Winful, Phys. Rev. Lett. 90 (2003) 023901.
[67] M. Büttiker, S. Washburn, Nature 422 (2003) 271.
[68] H. Winful, Nature 424 (2003) 638.
[69] A.M. Steinberg, P.G. Kwiat, R.Y. Chiao, Phys. Rev. Lett. 71 (1993) 708–711.